



OPEN

Design and optimization of hollow microneedle spacing for three materials using finite element methods

Xiaodan Zhang¹, Qifei Gu¹, Xue Sui¹, Jie Zhang¹, Jingwei Liu² & Rui Zhou^{1✉}

The main advantages of microneedles are precise drug delivery through human skin, minimal tissue damage and painlessness. We conducted structural analysis and skin puncture studies of hollow microneedles using ANSYS for three materials: Hafnium Dioxide (HfO_2), Polyglycolic acid (PGA) and Polylactic acid (PLA). Firstly, we selected three lengths, three tip diameters and three base diameters to conduct a $L_9(3^4)$ orthogonal experiment. Thus, we obtained nine different single-needle structures for each material, totaling 27 models for three materials. Subsequently, we investigated the stability and puncture properties of single needles. The optimal structures of the single-needle for three materials were same. Then, we used the optimal structure of the single-needle to establish the double-needle, triple-needle and five-needle models with ten different spacings. The simulations were carried out to examine the maximum stress during puncture. Finally, we investigated the hydrodynamic properties of water and lidocaine ibuprofen [*Lid*][*Ibp*] in the lumen of the microneedle. The results indicated that the optimal spacing of multi-needles varies depending on the material. The flow velocity of the fluid in the lumen is positively correlated with the pressure. Increasing the pressure can effectively reduce the flow velocity loss of low-viscosity fluid.

Keywords Hollow microneedle, Finite element analysis, Skin model, Spacing design, Mechanical strength, Puncture force

Microneedles (MNs) represent novel approaches in transdermal drug delivery systems. It can puncture the epidermal layer of the skin, forming tiny pores through which the drug can reach a specific site to play a therapeutic effect. This method can improve the rate of drug absorption and shorten the time of drug delivery¹. Compared to intradermal injection, microneedles have smaller structural dimensions, less pain, less bleeding, less skin damage and faster healing, which makes microneedles the ideal method of transdermal drug delivery².

According to the mode of drug delivery, microneedles can be divided into four types³. The first type is solid microneedles, which are inserted into the skin and then removed, while the drug is applied to the area punctured by the microneedle to deliver the drug⁴. The second type is coated microneedles, which are covered with drug coating on the surface and the drug coating can be dissolved and released rapidly after piercing into the skin⁵. The third type is dissolving microneedles, made of biodegradable material and dissolves itself by contacting interstitial fluid after insertion into the skin, thus releasing the drug⁶. The fourth type is hollow microneedles, which have an internal cavity structure⁷ and the bottom of the microneedles can be connected with pressure-driven devices to control the drug flow rate and realize slow and controlled release of the drug. Hollow microneedles can also be equipped with a drug reservoir to realize high-dose drug delivery⁸.

In the literature, many researchers have analyzed the materials which have been used to manufacture microneedles. Silicon was one of the materials and used to manufacture microneedles for a long time. Henny et al.⁹ used silicon to fabricate microneedles and were the first to use them in the transdermal drug delivery system in 1998. Due to the complexity of the manufacturing process, researchers have attempted to find more simpler methods for manufacturing silicon microneedles¹⁰. Silicon has good biocompatibility and is less likely to cause inflammatory reactions, but it is brittle and prone to fracture. Metallic materials have also been used to manufacture hollow microneedles in recent years¹¹. Yan et al.¹² manufactured stainless steel microneedles using chip and electrochemical corrosion methods, and the results showed that the microneedles of this material could successfully puncture the rats' skin and maintain the skin's overall integrity. Metals have high strength and

¹School of Chinese Materia Medica, Beijing University of Chinese Medicine, Beijing 102488, China. ²Capital University of Economics and Business, Beijing 100070, China. ✉email: rzhou_bucm@163.com

puncture ability. They are less biocompatible. It may cause severe adverse reactions in patients. With the rapid development of materials science, polymer materials such as polyvinyl alcohol (PVA), polylactic acid (PLA), etc., have been widely used as materials for the manufacture of microneedles because of their biocompatibility, toughness and ease of processing into various forms¹³. The inorganic material hafnium dioxide (HfO_2) has been applied in the medical field due to its low toxicity, stability and biocompatibility¹⁴, which has wide applications and can be used as a novel material for microneedles.

Clinically hollow microneedles can be used either as single or multiple needles. When used in a multi-needle format, the tip structures and spacings of microneedles are critical factors for the mechanical integrity and skin puncture of microneedles. Davis et al.¹⁵ found that the force required to puncture the skin increases approximately linearly with the tip area of the needle tip. Loizidou et al.¹⁶ studied the influence of the geometric composition of microneedles on their mechanical strength. The simulation of microneedle bases, including triangular, square and hexagonal, showed that the mechanical strength was linearly related to the number of vertices in the polygonal base. The spacing factor also effects on the force of microneedles puncturing the skin. Olatunji et al.¹⁷ found that the spacings of microneedles began to affect the puncture force when the spacing was less than 150 μm .

Hollow microneedles deliver drugs through the internal lumen. Therefore, it is necessary to investigate the fluid behavior of drugs in the lumen. Lidocaine ibuprofen with local anesthetic effect can shorten the onset time and prolong the duration of anesthesia, which has potential clinical applications. Current studies on microneedles delivering lidocaine ibuprofen are mainly in the form of dissolving microneedles^{18,19}, while hollow microneedles delivering lidocaine ibuprofen administration have been less studied. The hydrodynamic behavior of the drug in the lumen of hollow microneedle tubes is still unclear.

We performed structural analysis and skin puncture studies of hollow microneedles using ANSYS for three materials: HfO_2 , PGA and PLA. First, we chose three lengths, three tip diameters and three base diameters to undertake a $L_9(3^4)$ orthogonal experiment. We obtained nine different single-needle structures for each material, totaling 27 models for three materials. We investigated single needles' stability and puncture properties. The optimal structure of the single-needle for three materials were same. Then, we used the optimal structure of the single needle to establish the double-needle, triple-needle and five-needle models with ten different spacings. The simulations were carried out to investigate the maximum stress during puncture. Finally, the hydrodynamic properties of water and [Lid][Ibp] in the lumen of the microneedle were investigated.

Model design

Hollow microneedle model

We selected the conical shape as the tip structure²⁰. Most hollow microneedles have an opening at the tip. However, the tip opening affects the structural strength and is prone to drug clogging²¹. The two-side opening structure was selected for this study to minimize the clogging issue. The design of the hollow microneedle was shown in Fig. 1.

Hollow microneedles are commonly less than 1mm in length so as to avoid contacting nerve endings during skin puncture²². We used the orthogonal design of experiments (DOE) method to approach the study of multifactorial experiments. We identified the three factors, lengths, base diameters and tip diameters. We chose three parameters of microneedles with lengths L of 250 μm , 350 μm and 500 μm , three parameters of base diameters D_b of 150 μm , 200 μm and 250 μm and three parameters of tip diameters D_t of 10 μm , 20 μm and 30 μm , respectively. Then, we obtained nine groups of hollow microneedles through the $L_9(3^4)$ orthogonal experiment. The orthogonal table was shown in Table 1. The nine groups of hollow microneedles were shown in Table 2.

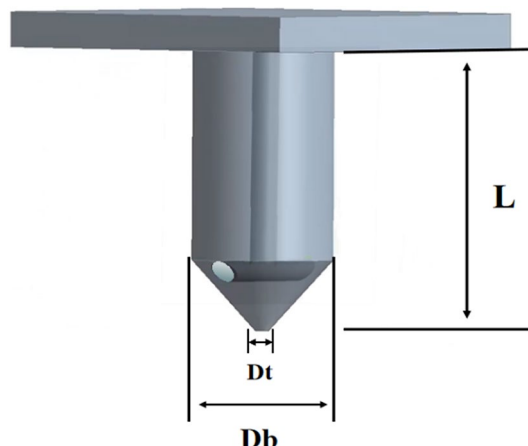


Fig. 1. Three-dimensional illustration of the hollow microneedle.

Factors	Level		
	1	2	3
Length L (μm)	250	350	500
Base diameter D_b (μm)	150	200	250
Tip diameter D_t (μm)	10	20	30

Table 1. The $L_9(3^4)$ orthogonal table.

Group	Parameter		
	Length L (μm)	Base diameter D_b (μm)	Tip diameter D_t (μm)
G1	250	150	10
G2	250	200	20
G3	250	250	30
G4	350	150	20
G5	350	200	30
G6	350	250	10
G7	500	150	30
G8	500	200	10
G9	500	250	20

Table 2. Structural parameters of 9 groups of hollow microneedles.

Material	Young's modulus (Gpa)	Poisson's ratio	Density (kg/m^3)
HfO_2^{23}	74.2	0.253	9680
PGA ²⁴	10	0.2	1560
PLA ²⁵	3.5	0.36	1251.5

Table 3. Mechanical properties of materials.

Skin part	Young's modulus E (MPa)	Poisson's ratio	Density (kg/m^3)	Skin resistance (MPa)
Stratum	120	0.39	1300	3.18
Active epidermis	5	0.48	1200	1.6
Dermis	0.5	0.48	1200	1.6

Table 4. Properties of the skin model²⁶.

Material selection

We selected three materials with low toxicity and biocompatibility that are widely used in the medical field: hafnium dioxide (HfO_2), polyglycolic acid (PGA) and polylactic acid (PLA). The physical and mechanical properties were shown in Table 3.

Skin model

We established a hyperelastic and isotropic skin model. Its parameters were shown in Table 4. The skin model was shown in Fig. 2. The expression for the hyperelastic and isotropic skin model was as follows.

$$W = C_{10}(I_1 - 3) \quad (1)$$

where W is the strain energy density, where I_1 is the first invariant of the Finger strain tensor B .

Structural mechanical analysis

The forces acting on the hollow microneedle during skin puncture were shown as follows.

- (1) Pressure: Hollow microneedles puncture the stratum corneum of the skin under pressure. The direction of pressure is along the axial direction. The maximum pressure that the hollow microneedle can withstand without failure is given by Eq. 2.²⁷

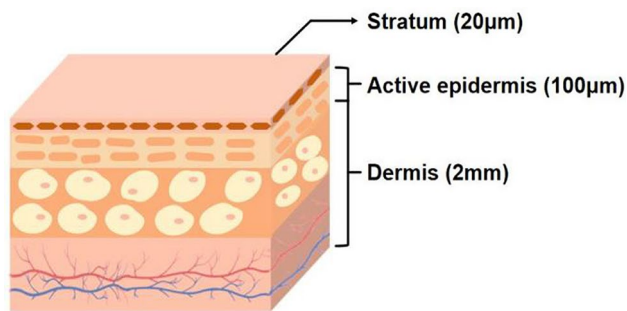


Fig. 2. Schematic of the skin structure.

$$F_{\max \text{ compressive}} = \sigma A_f \quad (2)$$

where σ represents the yield strength of the material, and A_f represents the cross-sectional area of the tip.

- (2) Skin resistance: Hollow microneedles are subjected to resistance from the skin as they are punctured into the skin. The skin resistance can be calculated by the following equation²⁸:

$$F_{\text{skin}} = P_{\text{piercing}} A_f \quad (3)$$

where P_{piercing} is the pressure required to puncture the stratum corneum, which was 3.18 MPa. The pressure decreases dramatically from 3.18 MPa to 1.6 MPa when the hollow microneedle punctures the stratum corneum²⁹.

- (3) Bending Force: Once the hollow microneedle punctures the skin, it cannot move freely sideways because the skin applies a bending force on it. The maximum bending force experienced by the hollow microneedle is expressed by Eq. 4;³⁰

$$F_{\max \text{bend}} = \frac{\sigma (I_1 + I_2)}{c L} \quad (4)$$

where c is the distance from the vertical axis to the outer edge, denoted as $c = D/2$. D is the outer diameter of the needle. L is the total length of the hollow microneedle.

I_1 is the moment of inertia for the cylindrical portion, which can be expressed as:

$$I_1 = \frac{\pi}{64} (D^4 - d^4) \quad (5)$$

where d is the inner diameter of the microneedle.

I_2 is the moment of inertia for the conical portion, which can be expressed as:

$$I_2 = \frac{D l^3}{396} \quad (6)$$

where l is the length of the conical portion.

- (4) S value: The S value of the microneedles was measured by the ratio of the fracture force to the piercing force. The safety of microneedles increases with the S value, which was calculated as follows.

$$S = \frac{F_{\text{fracture}}}{F_{\text{piercing}}} \quad (7)$$

where the $F_{piercing}$ was equal to 1/100 of F_{max} compressive. The $F_{fracture}$ was obtained by simulating. When the maximum stress in the microneedle reaches the yield strength of the material, the microneedle is considered to fracture, and the corresponding force at this point is the fracture force, i.e., $F_{fracture}$. The parameters were calculated in the equations in this section, shown in Table 5.

The results of structural mechanical analysis

This section studied the deformation of HfO_2 , PGA and PLA hollow microneedles. Axial and transverse loads were applied to the tip of the microneedles to investigate the hollow microneedles' structural strength. The results of the deformation of hollow microneedles with three materials were shown in Fig. 3. We can see that the deformation of the hollow microneedles with the three materials was obvious for G7. This structure of hollow microneedles has the longest length and the smallest base diameter, which cannot provide sufficient structural strength.

We analyzed the safety value (S value) of the microneedles. The S values were shown in Fig. 4. It can be seen that the S values of each material do not differ significantly with the same structure. The S values mainly depend on structures.

In order to select the optimal single-needle structure, we simulated the skin puncture of the single needle with HfO_2 , PGA and PLA materials. The friction coefficient between the microneedle and skin was set at 0.42³². A displacement constraint was applied to the hollow microneedle along the positive direction of the Y-axis, and fixed supports were applied to the skin's bottom and surrounding boundaries. The skin puncture model was shown in Fig. 5.

The results of single-needles with HfO_2 , PGA and PLA during puncture were shown in Table 6. We compared our results with experimental results in the literature. The trend of our force-displacement curve agree with the experimental curves in the literature³³. Figure 6 shows the comparison of simulation and experimental results of force-displacement of microneedle.

σ (Mpa)	d (μm)	$P_{piercing}$ (Mpa)	(μm)	L (μm)	A_f (μm^2)	c (μm)	D (μm)	$F_{fracture}$ (μN)
(a) The parameters of HfO_2 hollow microneedle								
60	40	3.18	100	250	78.54	75	150	2853
				250	314.16	100	200	12295
				250	706.86	125	250	12782
				350	314.16	75	150	11345
				350	706.86	100	200	21547
				350	78.54	125	250	2752
				500	706.86	75	150	20244
				500	78.54	100	200	2651
				500	314.16	125	250	11623
(b) The parameters of PGA hollow microneedle								
90	40	3.18	100	250	78.54	75	150	4306
				250	314.16	100	200	18248
				250	706.86	125	250	19004
				350	314.16	75	150	16838
				350	706.86	100	200	32331
				350	78.54	125	250	4146
				500	706.86	75	150	30292
				500	78.54	100	200	4004
				500	314.16	125	250	17494
(c) The parameters of PLA hollow microneedle								
47	40	3.18	100	250	78.54	75	150	2232
				250	314.16	100	200	9752
				250	706.86	125	250	10108
				350	314.16	75	150	8942
				350	706.86	100	200	16914
				350	78.54	125	250	2153
				500	706.86	75	150	15901
				500	78.54	100	200	2084
				500	314.16	125	250	9087

Table 5. The list of parameters.

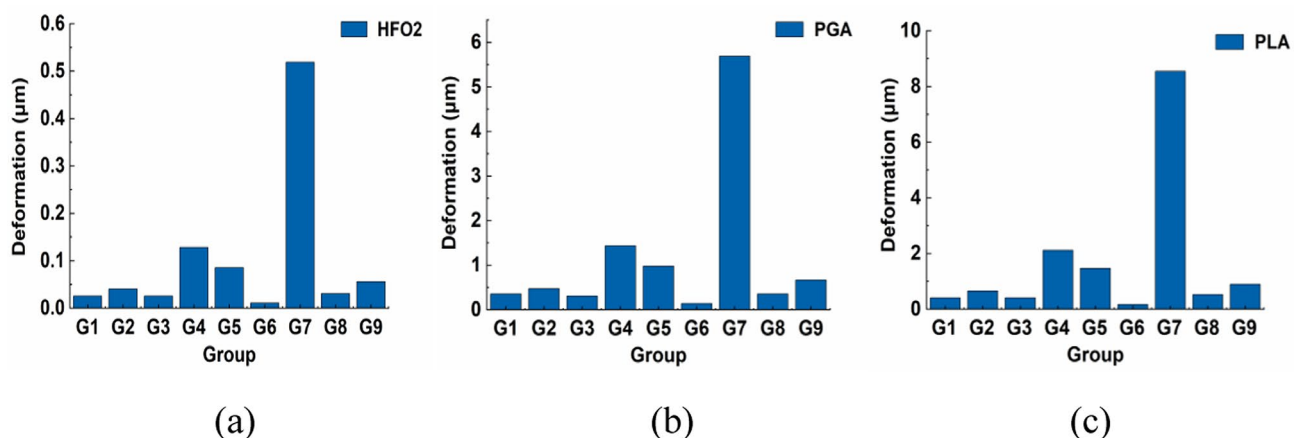


Fig. 3. Deformation of hollow microneedles of three materials (a) HfO_2 material. (b) PGA material. (c) PLA material.

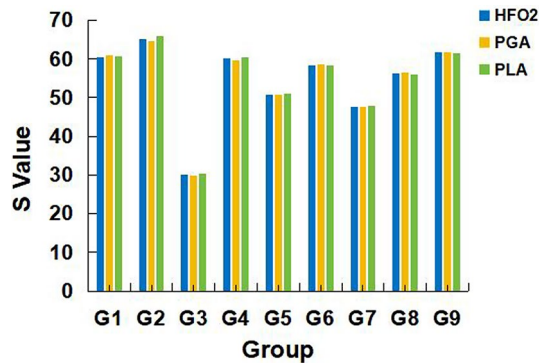


Fig. 4. S values of single-needle.

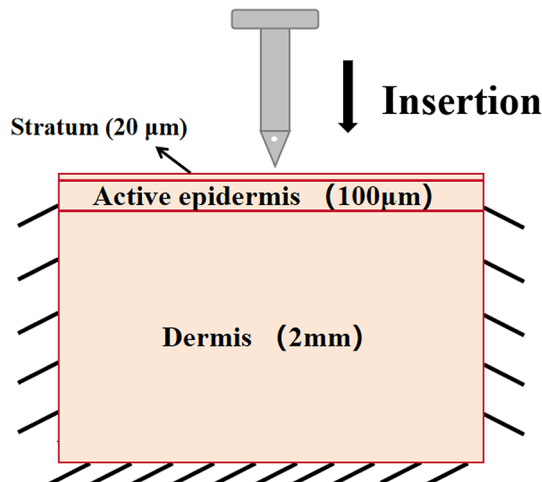
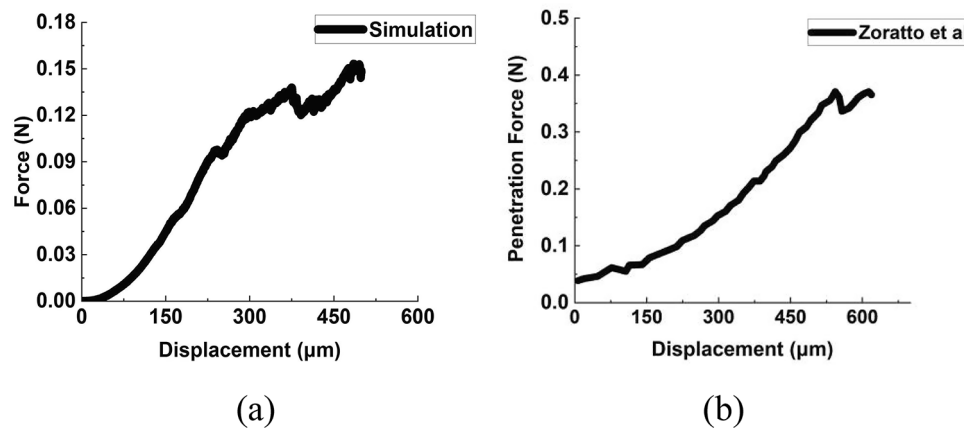
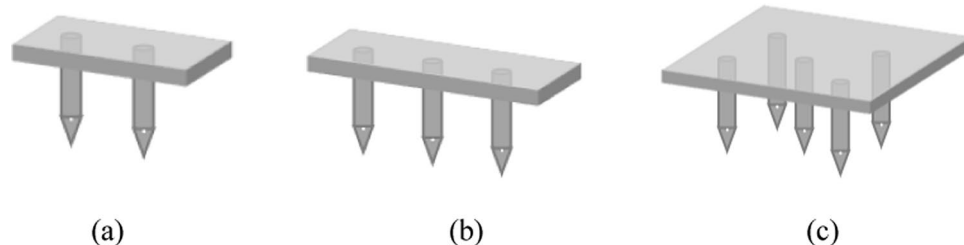


Fig. 5. Insertion illustration of single needle on skin.

Considering “not pass through” when the microneedle did not puncture the dermis. Considering “fracture” when the stress exceeded the yield strength of the material. Table 6 showed that the G9 successfully punctured the skin with three materials. It indicated that the hollow microneedle with a length of 500 μm , a base diameter of 250 μm , and a tip diameter of 20 μm is the most reasonable and optimal structure.

Group	Material		
	HfO ₂	PGA	PLA
G1	Not pass through	Not pass through	Not pass through
G2	Not pass through	Not pass through	Not pass through
G3	Fracture	Not pass through	Not pass through
G4	Not pass through	Pass through	Pass through
G5	Not pass through	Pass through	Pass through
G6	Not pass through	Fracture	Pass through
G7	Pass through	Pass through	Pass through
G8	Pass through	Pass through	Fracture
G9	Pass through	Pass through	Pass through

Table 6. Results of single-needle puncture.**Fig. 6.** The force-displacement curve. (a) the simulation result. (b) the result in literature by Zoratto et al.**Fig. 7.** 3D models of multi-needle (a) double-needle. (b) triple-needle. (c) five-needle.

The results of multi-needle during puncture

We used the parameters of G9 to establish the double-needle, triple-needle and five-needle models for each material, namely HfO₂, PGA and PLA. Then, we carried out the simulations to investigate the maximum stress of the models during puncture. The 3D models of double-needle, triple-needle and five-needle were shown in Fig. 7.

The HfO₂ double-needle model was used to investigate the maximum stress at spacings in the range of 300–1200 μm and the stress variation was shown in Fig. 8. The yield strength of HfO₂ is 60 MPa. We found that with the spacing of 300 μm, the maximum stress exceeded the yield strength of the material by the double-needle during puncture. Therefore, the structure of the double-needle with a spacing of 300 μm was considered a failure structure. When the spacings were in the range of 400–1200 μm, the HfO₂ double-needle could effectively puncture. Among them, the lowest stress occurs at the spacing of 500 μm with 12.938 Mpa. Because of the lowest stress, the 500 μm spacing design was considered as the optimal design for the HfO₂ double-needle.

The HfO₂ triple-needle model was used to investigate the maximum stress at spacings in the range of 300–1200 μm and the stress variation was shown in Fig. 9. The results showed that with the spacing of 300 μm, the maximum stress exceeded the yield strength of the material during puncture. When spacings were in the range

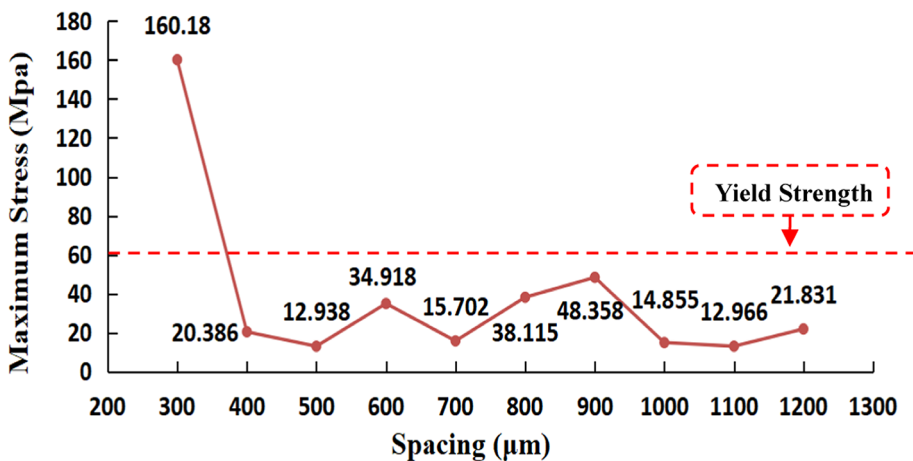


Fig. 8. Maximum Stress of HfO_2 double-needle with different spacings.

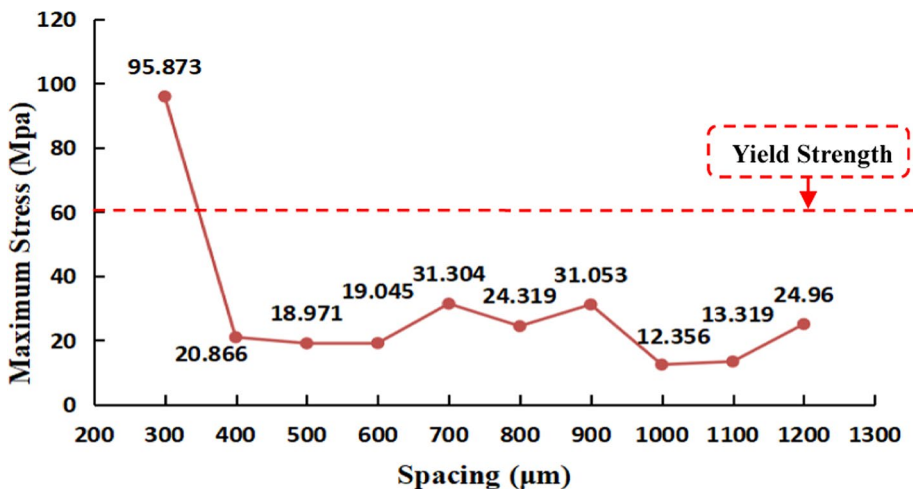


Fig. 9. Maximum Stress of HfO_2 triple-needle with different spacings.

of 400–1200 μm , the HfO_2 triple-needle could effectively puncture. The maximum stress in the range of 400–1200 μm was much lower than the yield strength of the material. Among them, the lowest stress occurs at the spacing of 1000 μm with 12.356 Mpa. Because of the lowest stress, the 1000 μm spacing design was considered as the optimal design for the HfO_2 triple-needle.

We used the HfO_2 five-needle model to investigate the maximum stress at spacings in the range of 400–1200 μm . The stress variation was shown in Fig. 10. We found that the maximum stress of the five-needle exceeded the yield strength of the material with spacings in the range of 600–1100 μm during puncture. Therefore, the structures of the five-needle with spacings of 600–1100 μm were considered failure structures. With spacings of 400 μm , 500 μm and 1200 μm , the five-needle could effectively puncture. The maximum stress was much lower than the yield strength of the material. Among them, the lowest stress occurs at the spacing of 500 μm with 21.833 Mpa. Because of the lowest stress, the 500 μm spacing design was considered as the optimal design for the HfO_2 five-needle.

The PGA double-needle was used to investigate the maximum stress at spacings in the range of 300–1200 μm and the stress variation was shown in Fig. 11. The yield strength of the PGA material is 90 MPa. With the spacing of 1100 μm , the maximum stress exceeded the yield strength of the material during puncture. Therefore, the structure of the double-needle with a spacing of 1100 μm was considered a failure structure. In all effective models, the lowest stress occurs at the spacing of 600 μm with 7.5821 Mpa. Because of the lowest stress, the 600 μm spacing design was considered as the optimal design for the PGA double-needle.

The PGA triple-needle was used to investigate the maximum stress with spacings in the range of 300–1200 μm and the stress variation was shown in Fig. 12. We found that with spacings of 300 μm and 800 μm , the maximum stress exceeded the yield strength of the material. Therefore, the structures of the triple-needle with spacings of 300 μm and 800 μm were considered failure structures. The maximum stress with spacings of 400 μm ~ 700 μm and 900 μm ~ 1200 μm did not exceed the yield strength of the material. Among them, the lowest stress

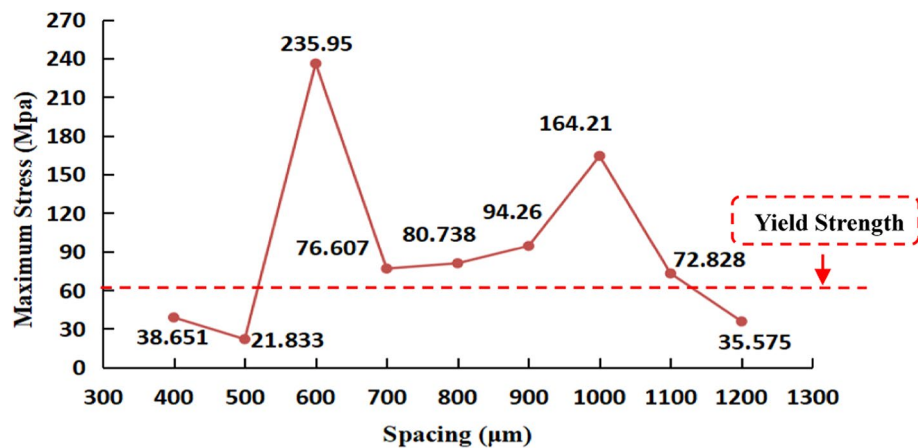


Fig. 10. Maximum Stress of HfO_2 five-needle with different spacings.

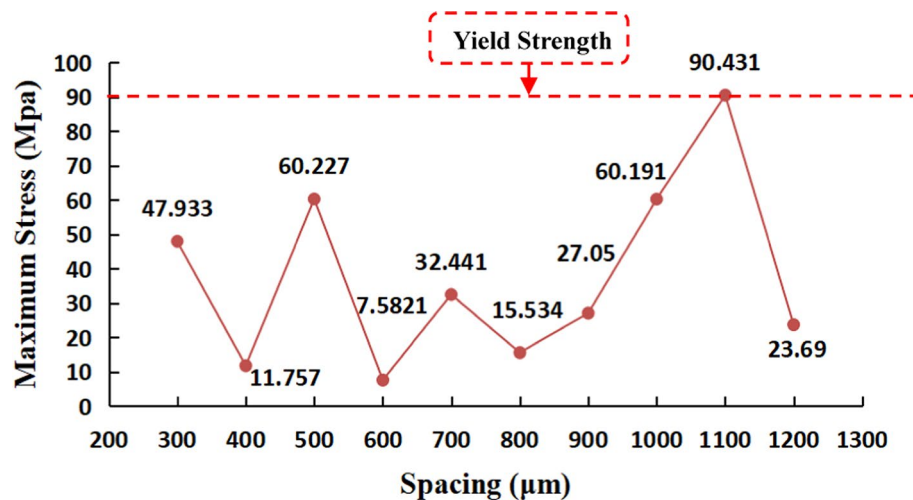


Fig. 11. Maximum Stress of PGA double-needle with different spacings.

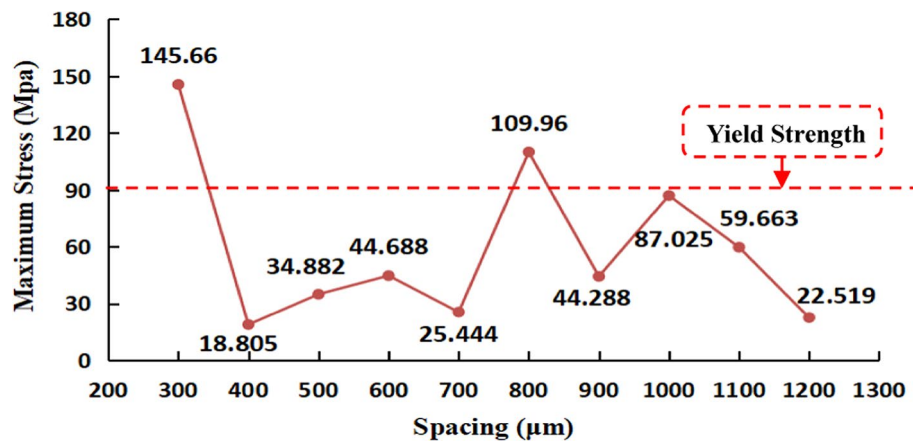


Fig. 12. Maximum Stress of PGA triple-needle with different spacings.

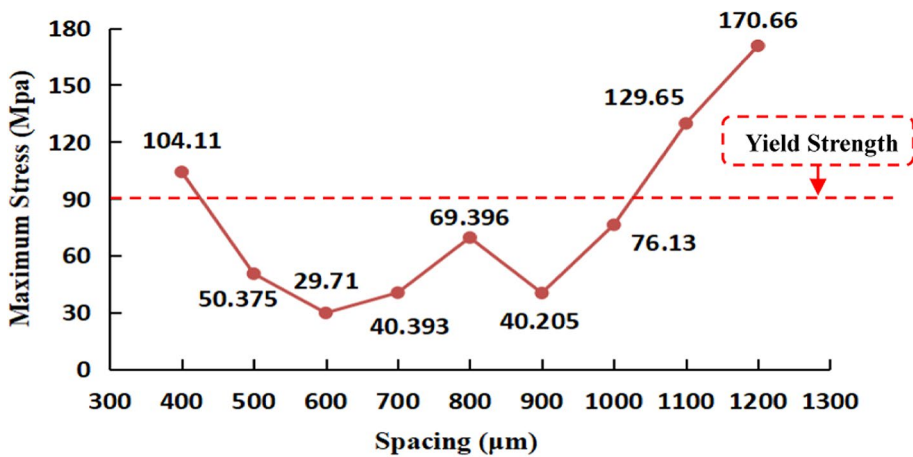


Fig. 13. Maximum Stress of PGA five-needle with different spacings.

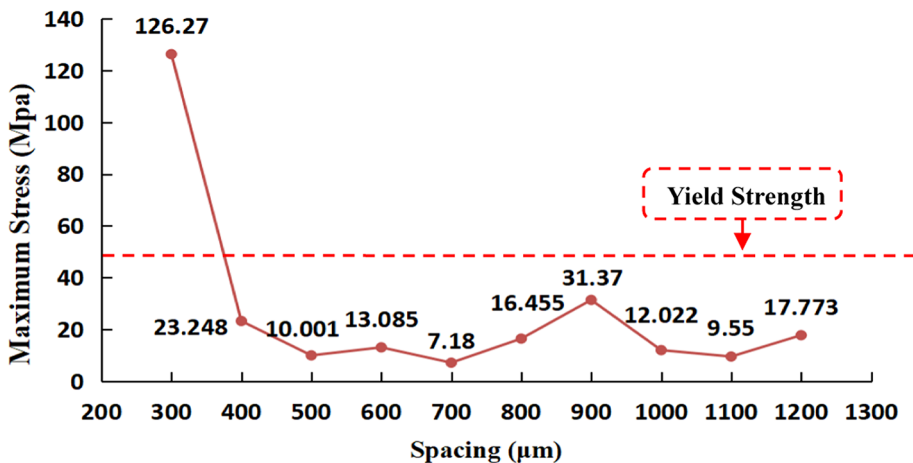


Fig. 14. Maximum Stress of PLA double-needle with different spacings.

occurs at the spacing of 400 μm with 18.805 Mpa. Because of the lowest stress, the 400 μm spacing design was considered as the optimal design for the PGA triple-needle.

We used the PGA five-needle to investigate the maximum stress with spacings in the range of 400–1200 μm . The stress variation was shown in Fig. 13. We found that the maximum stress exceeded the yield strength of the material with spacings of 400 μm , 1100 μm and 1200 μm . Therefore, the structures of the five-needle with spacings of 400 μm , 1100 μm and 1200 μm were considered failure structures. The maximum stress in the range of 500 μm –1000 μm did not exceed the yield strength of the material during puncture. Among them, the lowest stress occurs at the spacing of 600 μm with 29.71 Mpa. Because of the lowest stress, the 600 μm spacing design was considered as the optimal design for the PGA five-needle.

The PLA double-needle was used to investigate the maximum stress at spacings in the range of 300 μm ~ 1200 μm and the stress variation was shown in Fig. 14. The yield strength of the PLA material is 47 MPa. It was found that with the spacing of 300 μm , the maximum stress exceeded the yield strength of the material. Therefore, the structure with a spacing of 300 μm was considered a failure structure. The maximum stress was lower than the yield strength of the material with spacings of 400–200 μm during puncture. Among them, the lowest stress occurs at the spacing of 700 μm with 7.18 Mpa. Because of the lowest stress, the 700 μm spacing design was considered as the optimal design for the PLA double-needle.

The PLA triple-needle was used to investigate the maximum stress at spacings in the range of 300 μm ~ 1200 μm . The stress variation was shown in Fig. 15. We found that the maximum stress exceeded the yield strength of the material when spacings were 300 μm , 900 μm , 1000 μm , 1100 μm and 1200 μm . Therefore, the structures with spacings of 300 μm , 900 μm , 1000 μm , 1100 μm and 1200 μm were considered failure structures. The maximum stress with spacings in the range of 400 μm ~ 800 μm did not exceed the yield strength of the material during puncture. Among them, the lowest stress occurs at the spacing of 700 μm with 10.198 Mpa. Because of the lowest stress, the 700 μm spacing design was considered as the optimal design for the PLA triple-needle.

We used the PLA five-needle to investigate the maximum stress with spacings in the range of 400 μm ~ 1200 μm . The stress variation was shown in Fig. 16. We found that with spacings of 400 μm and 800 μm , the maximum

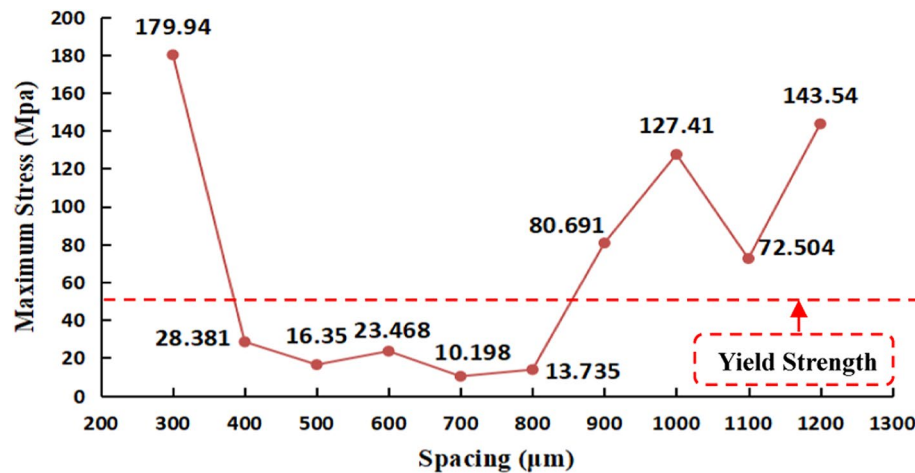


Fig. 15. Maximum Stress of PLA triple-needle with different spacings.

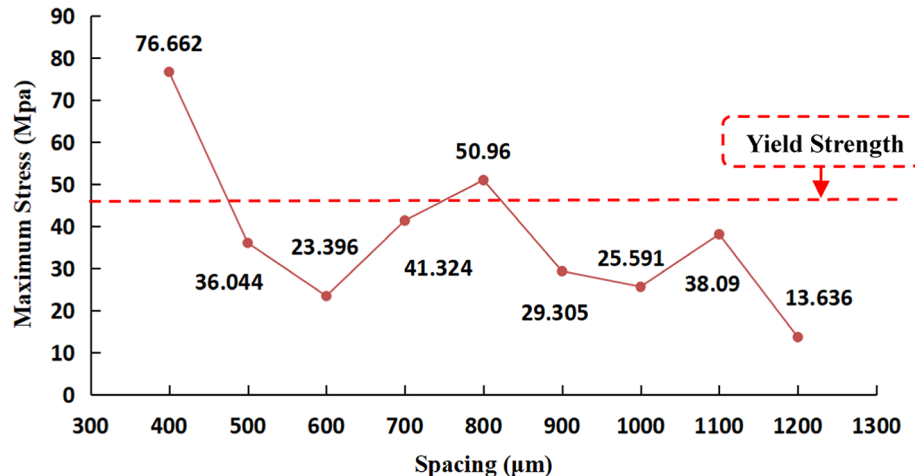


Fig. 16. Maximum Stress of PLA five-needle with different spacings.

stress exceeded the yield strength of the material. Therefore, the structures with spacings of 400 μm and 800 μm were considered failure structures. The maximum stress with spacings of 500 μm ~700 μm and 900 μm ~1200 μm was lower than the yield strength of the material during puncture. Among them, the lowest stress occurs at the spacing of 1200 μm with 13.636 MPa. Because of the lowest stress, the 1200 μm spacing design was considered as the optimal design for the PLA five-needle.

In summary, HfO₂, PGA and PLA hollow microneedles failed when the spacing was 300 μm . When the structures and numbers of microneedles were the same, the optimal spacing among the three materials had a significant difference, which was unexpected. The results are as follows. The optimal spacing for HfO₂ was 500 μm for double-needle, 1000 μm for triple-needle and 500 μm for five-needle. The optimal spacing for PGA was 600 μm for double-needle, 400 μm for triple-needle and 600 μm for five-needle. The optimal spacing for PLA was 700 μm for double-needle, 700 μm for triple-needle and 1200 μm for five-needle.

Fluid dynamic analysis

To study the hydrodynamic behavior of fluid in the internal lumen of hollow microneedles, the fluid domain of the lumen needs to be studied first. The boundary conditions of the inlet, outlet 1, outlet 2 and wall were set for the fluid domain model, as shown in Fig. 17. The fluid in the lumen is water and lidocaine ibuprofen (*[Lid]/[Ibp]*). The density and viscosity coefficient of water are $0.997 \times 10^3 \text{ kg/m}^3$ and $0.8949 \times 10^{-3} \text{ Pa}\cdot\text{s}$, respectively. The density and viscosity coefficient of *[Lid]/[Ibp]* are $1.02145 \times 10^3 \text{ kg/m}^3$ and $5606.9 \times 10^{-3} \text{ Pa}\cdot\text{s}$, respectively³². Pressures of 10 kPa, 30 kPa, 50 kPa, 70 kPa and 90 kPa were applied to the inlet to investigate the flow velocity changes, vortex generation and flow loss of the fluid in the hollow lumen.

The Reynolds number specifies the type of flow, which is expressed as:

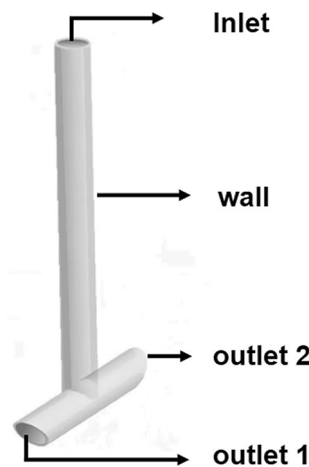


Fig. 17. Fluid domain model and boundary conditions.

$$Re = \frac{\rho d V}{\mu} \quad (8)$$

where ρ represents the density of the fluid, d represents the diameter of the lumen, V represents the velocity of the fluid in the lumen and μ represents the viscosity coefficient of the fluid. In this paper, we assume that the fluid is incompressible. The fluid flow is in laminar conditions ($Re < 2300$).

ANSYS Fluent was used to study the hydrodynamic properties of water and $[Lid]/[Ibp]$. The pressure variations were shown in Fig. 18. We found that the pressure of fluid was the highest at the inlet and the lowest at the intersection of the lumen. The velocity variations were shown in Fig. 19. We found that the initial velocity of fluid increased with increasing pressure at the inlet. The fluid flowed at a steady velocity from the axial lumen to the transverse lumen under different pressures. When passing through the 90° corner of the lumen, the transverse wall blocked the flow of fluid and the velocity of fluid decreased to zero rapidly. Due to friction between the fluid and the wall of the lumen, the fluid ultimately flowed out of the lumen at a smaller velocity. It can be seen from Fig. 19 that the velocity of the fluid varied with viscosity. Since the viscosity of $[Lid]/[Ibp]$ is significantly greater than that of water, its velocity within the lumen is extremely low.

We obtained the velocity streamline diagram of water in the lumen through simulation, as shown in Fig. 20. We found that vortices generated at the corners of the lumen under five pressure conditions: 10 kpa, 30 kpa, 50 kpa, 70 kpa and 90 kpa. The velocity streamlines of $[Lid]/[Ibp]$ in the lumen were shown in Fig. 21. We found that the flow of $[Lid]/[Ibp]$ was relatively stable in the lumen without vortex. The reason is that $[Lid]/[Ibp]$ flows from the inlet to the intersection at a very low velocity, which makes the $[Lid]/[Ibp]$ more easily change the flow direction to transverse. The possibility of vortex generation is reduced, so the flow is stable.

In order to examine the effect of pressure on the velocity loss, we calculated the velocity loss from the inlet to the outlet. The results were shown in Fig. 22. We found that increasing pressure can reduce the velocity loss of water. However, the velocity loss of $[Lid]/[Ibp]$ was not sensitive to the changes of pressure. The viscosity of water (0.8949×10^{-3} Pa·s) is significantly less than $[Lid]/[Ibp]$ (5606.9×10^{-3} Pa·s). Increasing the pressure can reduce the velocity loss of low-viscosity fluid rather than that of high-viscosity fluid.

Conclusion

In this study, we performed structural analysis and skin puncture studies of hollow microneedles using ANSYS for three materials: HfO_2 , PGA and PLA. First, we chose three lengths, three tip diameters and three base diameters to undertake a $L_9(3^4)$ orthogonal experiment. We obtained nine different single-needle structures for each material, totaling 27 models. Then, we investigated single needles' stability and puncture properties. The optimal structure of the single-needle was obtained. We found that the optimal structure of the single-needle for each material was the same. Then, we used the optimal structure of single-needle to establish the double-needle, triple-needle and five-needle models with ten different spacings. The simulations were carried out to investigate the maximum stress during puncture. Finally, the hydrodynamic properties of water and $[Lid]/[Ibp]$ in the lumen of the microneedle were investigated.

This study presents several significant findings. In the simulation of single-needle puncture, it was observed that the structure demonstrates material-independent properties. Despite the differences in the three materials, the optimal single-needle structure remained the same. In the multi-needle study, the optimal spacing depends on the material properties. Fluid dynamics studies have shown that the fluid's flow velocity in the lumen is positively correlated with the pressure. High-viscosity fluid is more stably in the lumen. Increasing the pressure can effectively reduce the flow velocity loss of low-viscosity fluid.

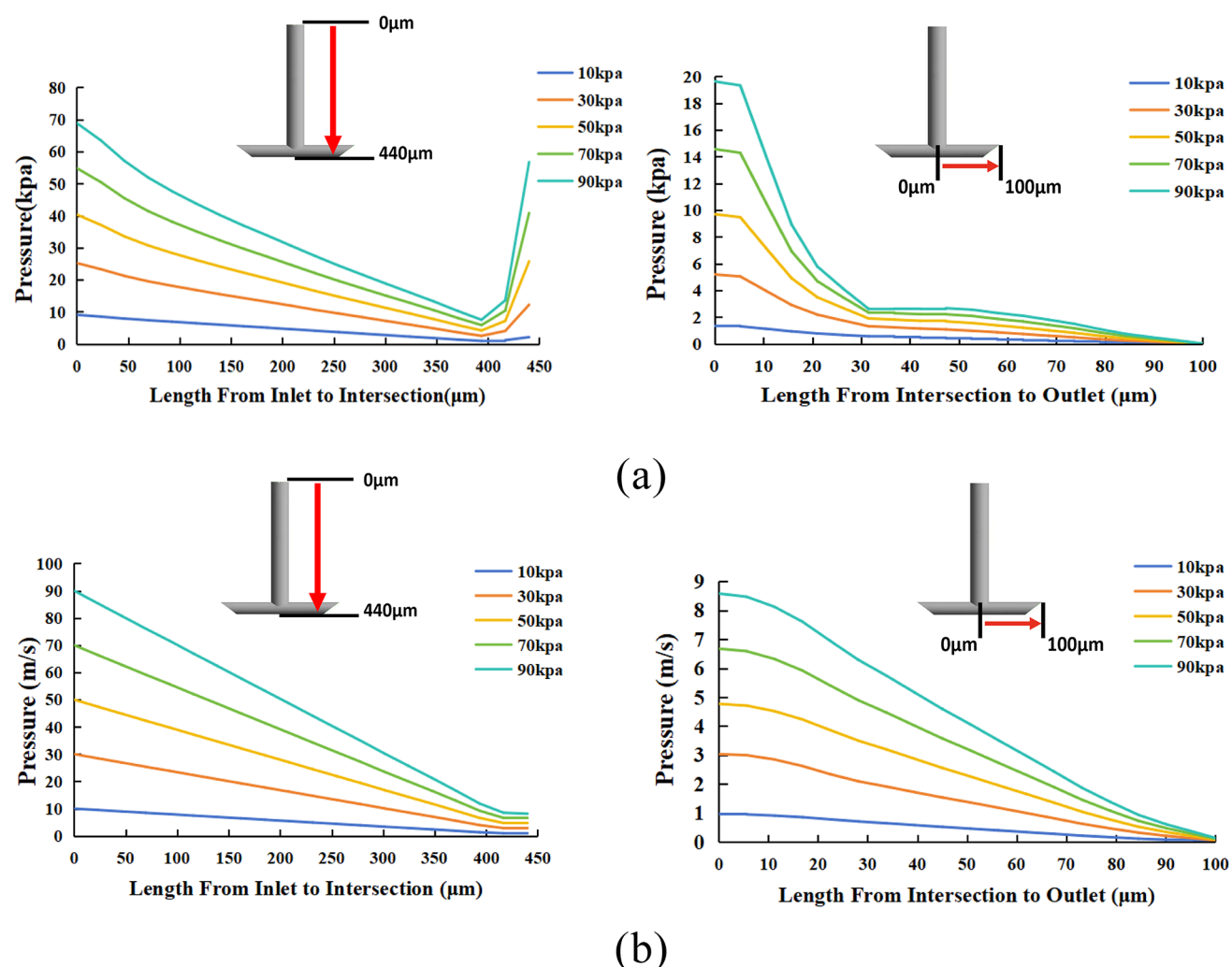


Fig. 18. Pressure variation diagram from inlet to one side outlet **(a)** Pressure diagram of water. **(b)** Pressure diagram of $[Lid]/[Ibp]$.

This research highlights the importance of considering material properties and spacing effects in the design of multi-needle structures. It also provides valuable insights for further research on optimizing microneedle designs for different applications and enhancing drug delivery efficiency.

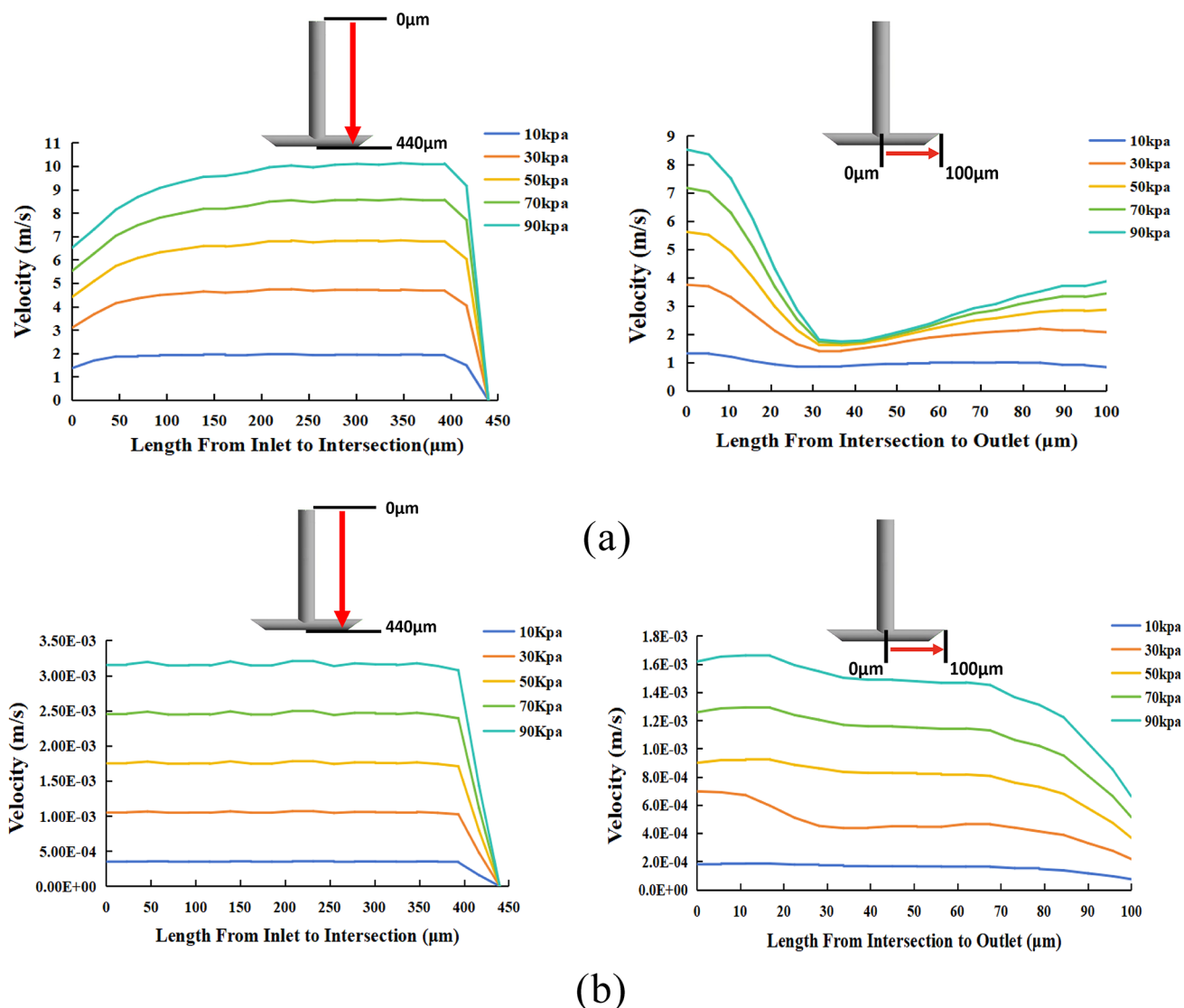


Fig. 19. Velocity variation diagram from inlet to one side outlet (a) Velocity diagram of water. (b) Velocity diagram of [Lid]/[Ibp].

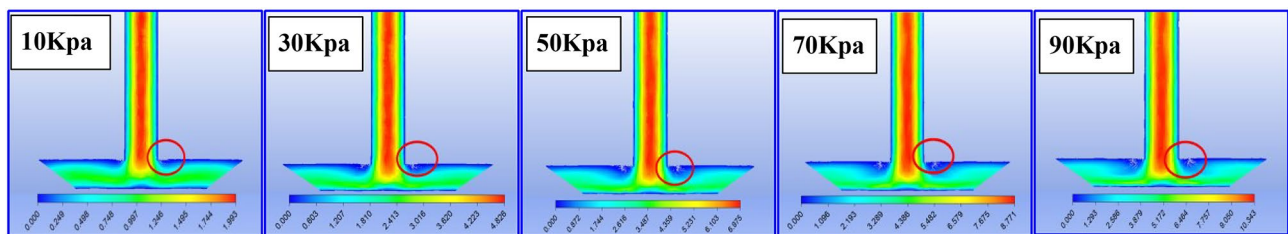


Fig. 20. Velocity streamlines of water under different pressure conditions.

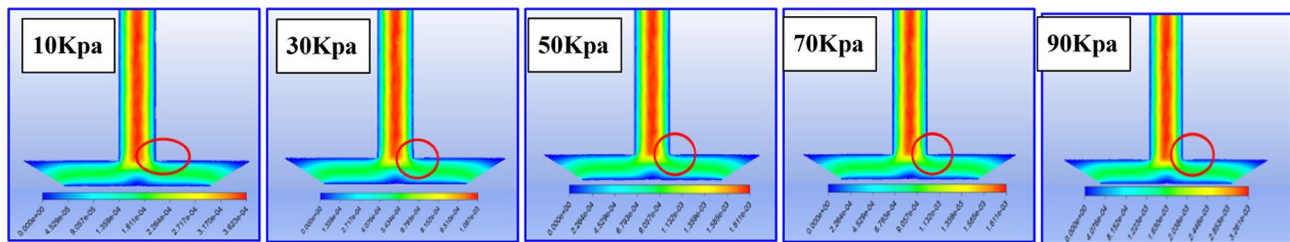


Fig. 21. Velocity streamlines of $[Lid]/[lbp]$ under different pressure conditions.

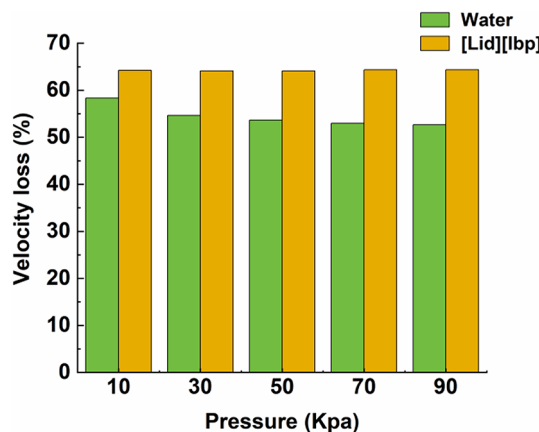


Fig. 22. The velocity loss of the fluid.

Data availability

The datasets generated during and/or analysed during the current study are available from the corresponding author on reasonable request.

Received: 16 May 2024; Accepted: 6 December 2024

Published online: 03 January 2025

Reference

- Ramadon, D. et al. Enhancement strategies for transdermal drug delivery systems: Current trends and applications. *Drug Deliv. Transl. Res.* **12**(4), 758–791 (2021).
- Nagarkar, R. et al. A review of recent advances in microneedle technology for transdermal drug delivery. *J. Drug Deliv. Sci. Technol.* **59**, 101923 (2020).
- Al-Nimry, S. S. & Daghmash, R. M. Three dimensional printing and its applications focusing on microneedles for drug delivery. *Pharmaceutics* **15**(6), 1597 (2023).
- Tariq, N., Ashraf, M. W. & Tayyaba, S. A review on solid microneedles for biomedical applications. *J. Pharmaceut. Innovat.* **17**(4), 1464–1483 (2022).
- Liu, F. et al. Protection of nanostructures-integrated microneedle biosensor using dissolvable polymer coating. *ACS Appl. Mater. Interf.* **11**(5), 4809–4819 (2019).
- Min, H. S. et al. Shape of dissolving microneedles determines skin penetration ability and efficacy of drug delivery. *Biomater. Adv.* **145**, 213248 (2023).
- Sil, D. et al. Promising role of microneedles in therapeutic and biomedical applications. *J. Drug Delivery Sci. Technol.* **91**, 105273 (2023).
- Jin, X. et al. Insulin delivery systems combined with microneedle technology. *Adv. Drug Deliv. Rev.* **127**, 119–137 (2018).
- Henry, S. et al. Microfabricated microneedles: A novel approach to transdermal drug delivery. *J. Pharmaceut. Sci.* **87**(8), 922–925 (1998).
- O'Mahony, C. et al. Hollow silicon microneedles, fabricated using combined wet and dry etching techniques, for transdermal delivery and diagnostics. *Int. J. Pharmaceut.* **637**, 122888 (2023).
- Sachan, G. et al. Antimicrobial evaluation of metal microneedles made by local electrodeposition-based additive manufacturing on metal-coated substrates. *JOM* **75**(12), 5643–5651 (2023).
- Yan, X. X. et al. Analysis of process parameters and performance test for fabricating stainless-steel metal microneedles. *Sens. Mater.* **30**(6), 1333–1340 (2018).
- Juster, H., van der Aar, B. & de Brouwer, H. A review on microfabrication of thermoplastic polymer-based microneedle arrays. *Polym. Eng. Sci.* **59**(5), 877–890 (2019).
- Siboro, P. Y. et al. Harnessing HFO₂ nanoparticles for wearable tumor monitoring and sonodynamic therapy in advancing cancer care. *ACS Nano* **18**(3), 2485–2499 (2024).
- Davis, S. et al. Insertion of microneedles into skin: Measurement and prediction of insertion force and needle fracture force. *J. Biomech.* **37**, 1155–1163 (2004).

16. Loizidou, E. Z. et al. Evaluation of geometrical effects of microneedles on skin penetration by CT scan and finite element analysis. *Eur. J. Pharmaceut. Biopharmaceut.* **107**, 1–6 (2016).
17. Olatunji, O. et al. Influence of array interspacing on the force required for successful microneedle skin penetration: Theoretical and practical approaches. *J. Pharmaceut. Sci.* **102**(4), 1209–1221 (2013).
18. Yang, H. et al. Development of lidocaine-loaded dissolving microneedle for rapid and efficient local anesthesia. *Pharmaceutics* **12**(11), 1067 (2020).
19. Rad, Z. F., Prewett, P. D. & Davies, G. J. An overview of microneedle applications, materials, and fabrication methods. *Beilstein J. Nanotech.* **12**, 1034–46 (2021).
20. De Martino, S. et al. Effect of microneedles shape on skin penetration and transdermal drug administration. *Biomater. Adv.* **142**, 213169 (2022).
21. Ahmad, N. F. N., Ghazali, N. N. N. & Wong, Y. H. Mechanical and fluidic analysis of hollow side-open and outer-grooved design of microneedles. *Mater. Today Commun.* **29**, 102940 (2021).
22. Serrano-Castañeda, P. et al. Microneedles as enhancer of drug absorption through the skin and applications in medicine and cosmetology. *J. Pharmacy Pharmaceut. Sci.* **21**, 73–93 (2018).
23. Zhang, Y., Campbell, A. & Karthikeyan, S. Finite element analysis of hollow out-of-plane HfO₂ microneedles for transdermal drug delivery applications. *Biomed. Microdev.* **20**, 1–7 (2018).
24. Abubaker, S. S. & Zhang, Y. J. Optimization design and fabrication of polymer micro needle by hot embossing method. *Int. J. Precis. Eng. Manuf.* **20**(4), 631–640 (2019).
25. Bodhale, D. W., Nisar, A. & Afzulpurkar, N. Structural and microfluidic analysis of hollow side-open polymeric microneedles for transdermal drug delivery applications. *Microfl. Nanofl.* **8**, 373–392 (2010).
26. Mohammadi, H., Ebrahimian, A. & Maftoon, N. Fracture behaviour of human skin in deep needle insertion can be captured using validated cohesive zone finite-element method. *Comput. Biol. Med.* **139**, 104982 (2021).
27. Villota, I. et al. Microneedles: One-plane bevel-tipped fabrication by 3D-printing processes. *Molecules* **27**(19), 6634 (2022).
28. Ahmad, N. N., Ghazali, N. N. N. & Wong, Y. H. Mechanical and fluidic analysis of hollow side-open and outer-grooved design of microneedles. *Mater. Today Commun.* **29**, 102940 (2021).
29. Aggarwal, P. & Johnston, C. R. Geometrical effects in mechanical characterizing of microneedle for biomedical applications. *Sens. Actuat. B: Chem.* **102**(2), 226–234 (2004).
30. Sawon, M. A., & Samad M. F. Design and analysis of silicon carbide microneedle for transdermal drug delivery[C]//2020 IEEE Region 10 Symposium (TENSYMP). IEEE, pp 1343–1346 (2020).
31. Chen, J. et al. A minimally invasive hollow microneedle with a cladding structure: Ultra-thin but strong, batch manufacturable. *IEEE Trans Biomed Eng* **66**(12), 3480–3485 (2019).
32. Shu, W. et al. Insights into the mechanics of solid conical microneedle array insertion into skin using the finite element method. *Acta Biomaterialia* **135**, 403–413 (2021).
33. Zoratto, N. et al. A bioinspired and cost-effective device for minimally invasive blood sampling. *Adv. Sci.* **11**(18), 2308809 (2024).

Acknowledgments

We gratefully acknowledge the financial support from High-level Construction Discipline of State Administration of Traditional Chinese Medicine[zyydzk-2023272] and Beijing University of Chinese Medicine with Funds [2018-JYBZZ-JS020, 2020-JYB-ZDGG-50].

Author contributions

Conceptualization and methodology, X.Z. and R.Z.; software and data curation, Q. G. and X. S.; writing—editing and review, X. Z., Q. G. and J. L.; supervision, J. Z.; project administration, R.Z. All authors have read and agreed to the published version of the manuscript.

Date availability

The datasets generated during and/or analyzed during the current study are available from the corresponding author on reasonable request. We used ANSYS Screenshot, Photoshop, Origin 2024 and Microsoft Excel to create the figures.

Declarations

Competing interests

The authors declare no competing interests.

Additional information

Correspondence and requests for materials should be addressed to R.Z.

Reprints and permissions information is available at www.nature.com/reprints.

Publisher's note Springer Nature remains neutral with regard to jurisdictional claims in published maps and institutional affiliations.

Open Access This article is licensed under a Creative Commons Attribution-NonCommercial-NoDerivatives 4.0 International License, which permits any non-commercial use, sharing, distribution and reproduction in any medium or format, as long as you give appropriate credit to the original author(s) and the source, provide a link to the Creative Commons licence, and indicate if you modified the licensed material. You do not have permission under this licence to share adapted material derived from this article or parts of it. The images or other third party material in this article are included in the article's Creative Commons licence, unless indicated otherwise in a credit line to the material. If material is not included in the article's Creative Commons licence and your intended use is not permitted by statutory regulation or exceeds the permitted use, you will need to obtain permission directly from the copyright holder. To view a copy of this licence, visit <http://creativecommons.org/licenses/by-nc-nd/4.0/>.

© The Author(s) 2024